Basic Study on Vortex Ring State Detection of Multi-rotor UAV Using Motor Counter Torque Observer

Manto Kamiya, Sakahisa Nagai, Hiroshi Fujimoto
The University of Tokyo
5-1-5, Kashiwanoha, Kashiwa, Chiba, 277-8561, Japan
Corresponding author's e-mail: kamiya.manto22@ae.k.u-tokyo.ac.jp

***Abstract*—The descent phase of the multi-rotor Unmanned Aerial Vehicles (UAVs) is one of the situations when UAVs tend to lose their control because of the Vortex Ring State (VRS). The VRS is one of the states of turbulence. The VRS is a well-known phenomenon in manned helicopters and it can also occur during the descent of a UAV. It is difficult to escape from the VRS without taking the VRS recovery motion. Some previous studies have proposed to avoid the VRS condition. However, those methods do not consider the effect of the wind disturbance. It is important to know the real-time turbulence information and detect the VRS to be robust to unexpected wind. This paper proposes a novel VRS detection method using the counter torque of the propeller motor to obtain real-time turbulence information. The method is verified with the bench experiments in a wind tunnel. The results show the possibility of the proposed method to detect the airflow flows into a propeller from dangerous airflow angles.**

***Index Terms*—multi-rotor UAV, vortex ring state, observer, motor control, VRS avoidance**

I. Introduction

The UAVs have been expected to be used in a wide range of industrial fields [1]–[3]. The use of eVTOLs as public transportation is also considered by applying the technologies of UAVs, and this has been studied recently [4]. The recent development of UAVs reasons from the convenient features of UAVs. In particular, dexterity and agility are important characteristics of UAVs to conduct many tasks in industrial fields. On the other hand, some challenges regarding safety such as fault tolerance or robustness still exist and many studies have been carried out [5], [6]. Therefore, there are need for control methods which solve the problem of safety without compromising the convenient features of UAVs.

A. Challenges of descent motion of UAVs

The descent phase of the UAVs is one of the major situations where UAVs are likely to be unstable. The airflow becomes from below the propellers when UAVs are descending. This can cause some turbulence around the propellers of a UAV and it can lead the UAV to unstable or uncontrollable. The turbulence comprised of vortices can occur when the down-wash of a propeller collides with the airflow from below the propeller. This state of turbulence is called Vortex Ring State (VRS). This phenomenon is well-known in manned helicopters or tilt-rotor VTOLs. The phenomenon also occurs during the descent of a UAV. The thrust fluctuation and thrust loss are observed when the VRS occurs. It is usually difficult to recover from the VRS by increasing the rotational speed of the propeller because the energy of the propeller is absorbed by the turbulence. Therefore, real-time VRS detection and VRS recovery motion are necessary for a UAV to improve its robustness.

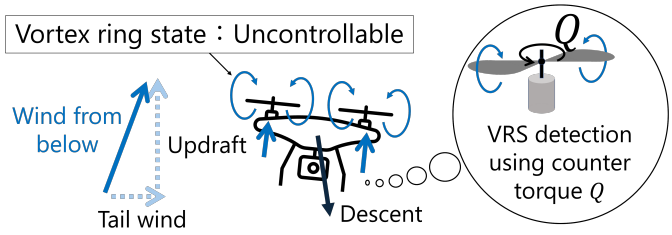

Fig. 1. The overview of the VRS detection.

B. Vortex Ring State (VRS)

VRS is one of the states of turbulence. As described in Fig. 1, the VRS occurs when the vertical airspeed from the back side of a propeller approaches the induced velocity of the propeller. At this condition, the recirculation through the propeller is created by upward airflow [7]. It is difficult to establish an analytically accurate model of the VRS because it is a kind of turbulence. Many studies have been conducted to find out the boundary of the VRS by focusing on the thrust and torque [7], [8]. Ref. [9] have proposed a method to find out the boundary condition of the vertical and horizontal airspeed of the VRS with a simple model.

1) ONERA VRS criterion: ONERA VRS criterion is one of the models to derive the VRS boundary by using the Wolkovitch VRS model and experimental results [9]. At the first step, the propeller thrust F_z and propeller slipstream velocity V_s are derived. Based on momentum and simple

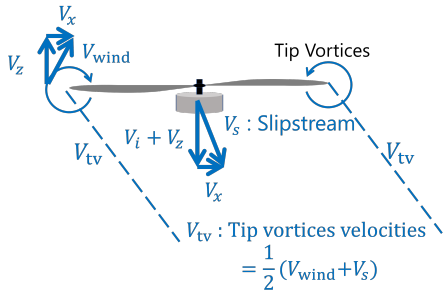

Fig. 2. The Wolkovitch model.

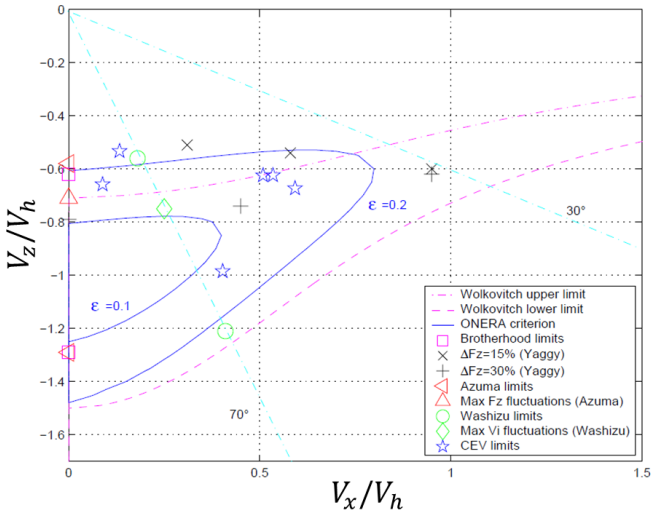

Fig. 3. The VRS boundary model of previous study [9].

vortex theory, F_z and V_s are described as follows [9]:

$$F_z = \frac{1}{2}\rho\pi D_{\text{p}}^2 V_s V_i, \tag{1}$$

$$V_s = \sqrt{V_x^2 + (V_i + V_z)^2}. \tag{2}$$

where ρ and D_{p} are air density and propeller diameter, respectively. V_x and V_z are horizontal and vertical airspeed in the UAV coordinate. V_i is induced velocity. The induced velocity at hovering V_h is calculated by

$$V_h = \sqrt{\frac{2F_z}{\rho\pi D_{\text{p}}^2}}. \tag{3}$$

(2) is non-dimensionalized by dividing both sides by hover induced velocity V_h to derive:

$$1 = \bar{\nu}^2(\bar{\mu}^2 + (\bar{\nu} + \bar{\eta})^2), \tag{4}$$

$$\bar{\nu} = \frac{V_i}{V_h}, \bar{\mu} = \frac{V_x}{V_h}, \bar{\eta} = \frac{V_z}{V_h}. \tag{5}$$

Then, the $\bar{\nu}$ is obtained when the $\bar{\mu}$ and $\bar{\eta}$ are given with appropriate interpolation and correction to be consistent with experimental results. The detailed explanation is included in [9]. In the next step, the conditions under which the VRS occurs are considered. According to the Wolkovitch model illustrated in Fig. 2, the VRS is caused by the interaction between tip vortices development and propeller blades. According to Fig. 2, the velocities of the tip vortices V_{tv} are calculated as

$$|V_{\text{tv}}| = \frac{1}{2}(V_{\text{wind}} + V_s) = \sqrt{V_x^2 + \left(\frac{V_i}{2} + V_z\right)^2}. \tag{6}$$

Therefore, the criterion based on the travel distance of the propeller tip vortices is defined by non-dimensionalizing (6) by hovering induced velocity V_h as follows:

$$\sqrt{\left(\frac{\bar{\mu}}{k_1}\right)^2 + \left(\frac{k_2\bar{\nu}}{2} + \bar{\eta}\right)^2} \leq \epsilon. \tag{7}$$

where k_1 and k_2 are fitting parameters. The meaning of (7) is that the turbulence occurs if the tip vortices velocities are less than ϵ. Fig. 3 shows the VRS boundary derived from (7) in [9]. The ONERA criterion ($\epsilon = 0.2$) in Fig. 3 is considered as a theoretical VRS boundary in this paper.

2) Previous studies of the VRS avoidance : The thrust fluctuation and thrust loss are observed when the VRS occurs and those affect the control performance significantly. Some studies have been carried out to deal with the phenomenon of UAVs. The previous studies are categorized as follows:

1) Generating the trajectories which are less likely to provoke VRS based on the VRS boundary map [10], [11]
2) Considering the optimal descent motion to avoid the VRS [12]–[14]
3) VRS detection or prediction [15]

Method 1) considers the VRS by introducing restrictions on the descending velocity and carries out the trajectory optimization by minimizing the cost function under the restriction. The most simple type of restriction is confining the vertical descent velocity v_z such as $-10 \leq v_z \leq 0$ [10]. Another type of restriction takes into account the VRS boundary map such as in Fig. 3. The method generates the horizontal velocity V_x and vertical velocity V_z not to enter the VRS area [11]. Method 2) proposes a novel descent motion to avoid the VRS. For example, ref. [12] proposes to use yaw rotation during the descending of a UAV. This method attempts to avoid the airflow flowing into the propellers from the dangerous airflow angle. However, these methods do not take into account the effect of wind disturbance. Therefore, they are not robust against wind disturbances such as updrafts or tailwinds. Method 3) attempts to detect turbulence by measuring the air pressure difference between above and below a UAV. This method can obtain real-time information of the airflow and turbulence. However, not only is the additional equipment required, but also it can not obtain information of the airflow around the propellers.

C. About this study

To avoid the VRS, control strategies such as restriction of the descent velocity are used for now. However, not only these control strategies still can have trouble when unexpected wind disturbance flows, but they also deteriorate agility and

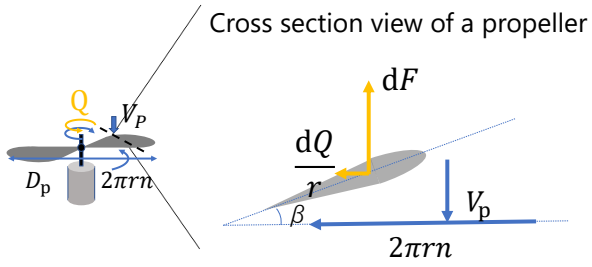

Fig. 4. Velocities and force acting on propeller blade element.

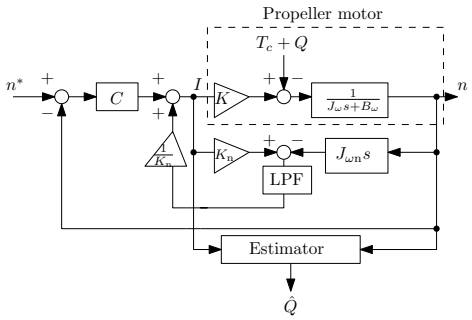

Fig. 5. Propeller motor counter torque Q estimator and propeller rotational speed n controller C.

dexterity by using conservative velocity restrictions.

A novel VRS detection method using motor counter torque is proposed in this study. The proposed method attempts to obtain real-time information of the turbulence around the propellers by utilizing motor information. Hence, this method has the potential to be used for VRS detection and VRS recovery to reinforce the robustness of the UAVs.

This paper is organized as follows: Section Ⅱ describes the modeling of a motor and a propeller. The new VRS detection method is proposed in Sections Ⅲ. The wind tunnel experiments of the VRS are discussed in Sections Ⅳ. Finally, the paper is concluded in Section Ⅴ.

II. Modeling of Motor and Propeller

In this section, the dynamics of the motor and propeller are focused on. The dynamics of the propeller is described with blade element theory. Fig. 4 shows the forces applied to the propeller. The equation of motion of the electric motor is described as follows:

$$T^* - Q = 2\pi J_\omega \frac{\mathrm{d}n}{\mathrm{d}t} + 2\pi B_\omega n + T_c, \tag{8}$$

where T^* is torque reference, J_ω is inertia moment of propeller, B_ω is viscosity coefficient of propeller, and T_c is coulomb friction. Q is counter torque which is applied in the opposite direction of the propeller rotation by the wind. n is the rotational speed of the propeller. Thrust F_z and counter torque Q of the propeller are described as follows:

$$F_z = C_F(J)\rho n^2 D_\mathrm{p}^4, \tag{9}$$
$$Q = C_Q(J)\rho n^2 D_\mathrm{p}^5. \tag{10}$$

ρ is air density and D_p is the propeller diameter. C_F is coefficient of thrust and C_Q is coefficient of torque. C_F and C_Q are often described as a function of advance ratio J which is defined as

$$J = \frac{V_p}{nD_\mathrm{p}}. \tag{11}$$

According to ref. [16] and equations (9) and (10), the relationship between F_z and Q can be obtained as

$$C_F = aC_Q + b, \quad F_z = a\frac{Q}{D_\mathrm{p}} + b\rho n^2 D_\mathrm{p}^4. \tag{12}$$

where a and b are coefficients obtained from the experiments.

III. Proposed Method of Vortex Ring State Detection

According to (12), there are physical relationship between the counter torque Q and propeller thrust F_z when the turbulence does not exist. From (12), we assumed that the information of the thrust F_z can be obtained from the counter torque Q even if turbulence occurs such as the VRS. The following proposed VRS detection method is based on this assumption.

The low frequency fluctuation of the thrust F_z is observed in the previous study when the VRS occurs [7]. Referring to this fact, the proposed method of VRS detection in this paper attempts to observe this characteristic of low-frequency fluctuation of F_z by using the counter torque estimation. There are three steps to detect the VRS with the proposed method.

A. Step1: Estimate counter torque of the propeller motor

In the first step, the observer-based counter torque Q estimation is conducted. The block diagram is shown in Fig. 5. Note that I is motor current and n is rotational speed. The Q can be estimated as follows:

$$\hat{Q} = \frac{1}{\tau_d s + 1}\left(K_\mathrm{n} I - 2\pi(J_{\omega\mathrm{n}} s + B_{\omega\mathrm{n}})n\right) - T_{c\mathrm{n}}. \tag{13}$$

Note that τ_d is the time constant of the low pass filter to guarantee the convergence of $\hat{Q}$. $J_{\omega\mathrm{n}}, B_{\omega\mathrm{n}}, T_{c\mathrm{n}}$ are the nominal value of J_ω, B_ω, T_c. K and K_n are the torque constant and nominal torque constant.

B. Step2: Conduct wavelet transformation of $\hat{Q}$

In the second step, the wavelet transformation of the estimated $\hat{Q}$ is conducted to analyze the both frequency domain and time domain of $\hat{Q}$. The wavelet transformation of $\hat{Q}$ is defined as

$$Q_W(t', F) = \int |F|^{-\frac{1}{2}} \hat{Q}(t) \overline{\Psi\left(\frac{t - t'}{F}\right)} \mathrm{d}t. \tag{14}$$

t' and F are parameters for the width of the time and frequency windows and $\overline{\Psi}$ is the mother wavelet that serves as the basis function. The Morse wavelet of the Matlab algorithm is used as the mother wavelet in this paper.

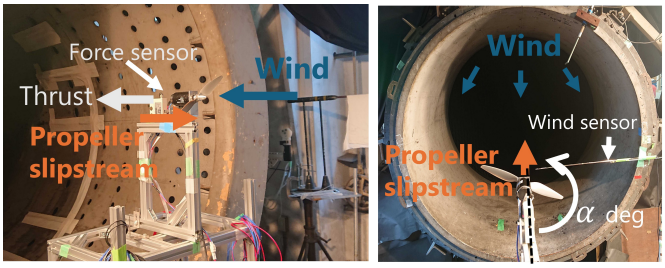

Fig. 6. Experimental setup

C. Step3: Integrate the low frequency area of Q_W as a feature value of the VRS

In the last step, the integrated value G in the low-frequency range of Q_W is calculated as a feature value of the VRS.

$$G = \int_{f_{c1}}^{f_{c2}} Q_W(t', F)\mathrm{d}F. \tag{15}$$

G indicates the magnitude of the low-frequency fluctuation. The frequency f_{c1} and f_{c2} and τ_d of the counter torque observer are determined based on the experimental results. If G exceeds the threshold G_{th} which is determined from the experimental results, the proposed method judges the situation as the VRS.

D. Proposal of the required speed of the VRS detection

The time limit of VRS detection should be defined to achieve recovery from the VRS. Let Z_{lim} be the acceptable vertical altitude loss from the beginning of the VRS. According to ref. [7], the maximum drop rate of the thrust is about 30%. Therefore, assuming the drop acceleration at the VRS is $0.3g$, the time T_{lim} to reach the drop distance Z_{lim} is calculated as follows:

$$T_{\text{lim}} = \frac{-v_{z0} + \sqrt{v_{z0}^2 + 0.6gZ_{\text{lim}}}}{0.3g} \tag{16}$$

where g is the gravity acceleration and v_{z0} is the initial vertical velocity at the beginning of the VRS. To discuss the specific value, let's consider the case when $Z_{\text{lim}} = 2\,\text{m}$, $g = 9.8\,\text{m/s}^2$ and $v_{z0} = 5\,\text{m/s}$ which is the common decent velocity of UAV. T_{lim} of this case is calculated as about $0.5\,\text{s}$ which can be considered as the time limit of the VRS detection.

IV. Experiments of Vortex Ring State Detection

Experiments were conducted in the wind tunnel to measure the VRS and to verify the proposed method. The propeller bench in Fig. 6 was used in the experiments. The $3\,\text{m/s}$ to $12\,\text{m/s}$ wind with every $1\,\text{m/s}$ flew into the propeller. The propeller thrust and counter torque were measured at $180°, 165°, 150°, 120°, 0°$ airflow angle α in Fig. 6. Each value was measured $10\,\text{s}$. τ_d of the counter torque $\hat{Q}$ estimator is set $0.01\,\text{s}$. The value of the wind sensor was used as the true value of wind velocity. IMADA 20N force sensor was used to measure the thrust. APC 10×4.5 MR propeller, Maxon DC motor, Maxon $10\,\text{bit}$ encoder, and Maxon motor driver ESCON70/10 were used. The other experimental conditions are shown in Table I.

TABLE I
Parameter in the Simulations.

Symbol	Definition	Value
J_ω	Inertia moment of propeller	$7.2 \times 10^{-5}\,\text{kgms}^2$
B_ω	Viscosity coefficient of propeller	$6.0 \times 10^{-6}\,\text{Nms/rad}$
T_c	Coulomb friction of motor	$1.5 \times 10^{-3}\,\text{N m}$
K	Torque constant	$30.2 \times 10^{-3}\,\text{Nm/A}$
D_p	Propeller diameter	$0.25\,\text{m}$
ρ	Air density	$1.2\,\text{kg/m}^3$

A. Experimental results of the wavelet transformation of the estimated counter torque $\hat{Q}$ and measured thrust F_z

The results of the wavelet transformation of the estimated counter torque $\hat{Q}$ and measured thrust F_z when the $8\,\text{m/s}$ wind flows from 180° and 0° airflow angle are shown in Fig. 7. As shown in Fig. 7, the magnitude at a low frequency around $10\,\text{Hz}$ of both counter torque $\hat{Q}$ and thrust F_z at 180° are stronger than the fluctuation at 0°. This is because the airflow from the back side of the propeller causes the VRS while airflow from the front side of the propeller has less influence on the turbulence. According to the result in Fig. 7(b) and time constant of the estimator of the $\hat{Q}$, the cutoff frequencies f_{c1} and f_{c2} for the feature value of (15) are determined as $1\,\text{Hz}$ and $10\,\text{Hz}$ in this paper.

B. Experimental results of the thrust and G at the VRS

The reduction rate of the thrust coefficient C_F, the increase rate of the standard deviation of the thrust coefficient $C_{F\text{std}}$, the calculated proposed VRS feature G at the wind tunnel experiment are shown in Fig 8. The reduction and increase rates are defined as

$$\bar{C}_F = \frac{C_F - C_{F0}}{C_{F0}},\ \bar{C}_{F\text{std}} = \frac{C_{F\text{std}} - C_{F\text{std0}}}{C_{F\text{std0}}}. \tag{17}$$

Note that C_{F0} and $C_{F\text{std0}}$ are the measured value of the thrust coefficient with no wind. C_F and $C_{F\text{std}}$ are measured values of the thrust coefficient at every airflow angle and wind velocity. These values are filtered with $10\,\text{Hz}$ low pass filter. In Fig. 8, the horizontal axis describe the wind velocity V_z non-dimensionalized by no wind induced velocity V_h.

In Figs. 8(a)–8(d), the areas where $\bar{C}_F$ is less than 0 are painted in blue as the areas of the VRS. The feature G using $10\,\text{s}$ of the data is plotted in Figs. 8(e)–8(h). The feature $G(0.5s)$ using $0.5\,\text{s}$ of data from $9\,\text{s}$ to $9.5\,\text{s}$ based on T_{lim} defined by (16) is also shown in Figs. 8(i)–8(l). Note that f_{c1} and f_{c2} for $G(0.5)$ were set to $7\,\text{Hz}$ and $10\,\text{Hz}$ in consideration of frequency resolution. The threshold G_{th} and $G_{\text{th}}(0.5s)$ which are set $9\times10^{-4}, 1.8\times10^{-3}$ on the basis of G and $G(0.5s)$ are also shown in Figs. 8(e)–8(l). In Figs. 8(e)–8(l), the areas where G exceeds G_{th} and $G_{\text{th}}(0.5s)$ are painted in blue. As can be seen in Figs. 8(a)–8(d), the thrust reduction and thrust fluctuation increase takes the maximum value at the same point $V_z/V_h = -1.2$ when the wind flows into

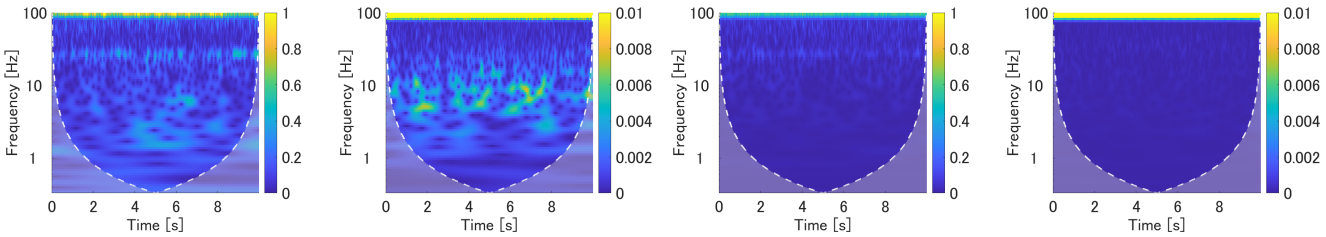

(a) F_z with airflow from 180° (b) $\hat{Q}$ with airflow from 180° (c) F_z with airflow from 0° (d) $\hat{Q}$ with airflow from 0°

Fig. 7. The wavelet transformation of propeller thrust F_z and estimated counter torque $\hat{Q}$.

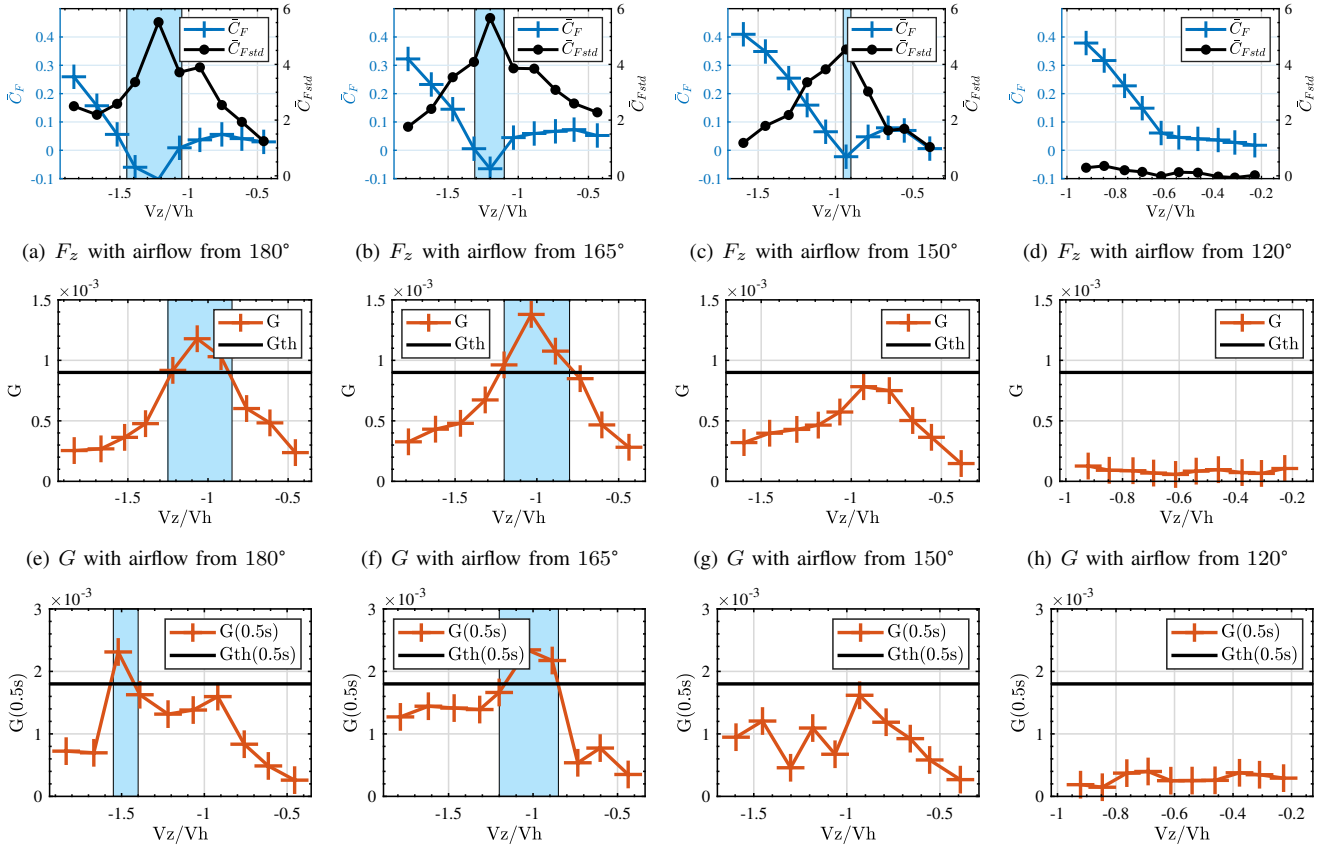

(a) F_z with airflow from 180° (b) F_z with airflow from 165° (c) F_z with airflow from 150° (d) F_z with airflow from 120°

(e) G with airflow from 180° (f) G with airflow from 165° (g) G with airflow from 150° (h) G with airflow from 120°

(i) $G(0.5\,\mathrm{s})$ with airflow from 180° (j) $G(0.5\,\mathrm{s})$ with airflow from 165° (k) $G(0.5\,\mathrm{s})$ with airflow from 150° (l) $G(0.5\,\mathrm{s})$ with airflow from 120°

Fig. 8. Thrust coefficient mean and standard deviation and the VRS feature value G.

the propeller at airflow angle 180° and 165°. This result is similar to the phenomenon observed at the VRS in the previous study [7]. It is noteworthy that thrust increases when V_z/V_h is smaller than -1.2. This thrust increase indicates the end of the VRS and the transition to the windmill brake state that is also observed in [17].

According to Figs. 8(e)–8(f), the proposed VRS feature value G takes the maximum value at $V_z/V_h = -1.0$. In addition, G decreases as the VRS disappears when the airflow angle is changed from 180° to 120°. The areas where G exceeds the threshold G_{th} and the areas where the $\bar{C}_F$ decreases have a common area partly in Figs. 8(a)–8(b) and Figs. 8(e)–8(f). G is also plotted in Fig. 9 and compared with the boundary of the $\epsilon = 0.2$ of the ONERA criteria with $k_1 = 4, k_2 = 1.24$ in section Ⅲ. According to Fig. 9, it can be seen that the area where the G is a large value is similar to the VRS area derived from the ONERA criteria. These results imply the correlation between G and VRS and the results verify the effectiveness of the proposed VRS detection method. On the other hand, $G(0.5s)$ has multiple peaks and different VRS detected areas from G, $\bar{C}_F$. This means that the proposed method has difficulty detecting VRS in a short period. The maximum thrust reduction is only 10 % in the experiments while about 30 % thrust reduction was observed in [9]. This is probably because the difference in the scale of the propeller is not taken into account completely even the dimensionless

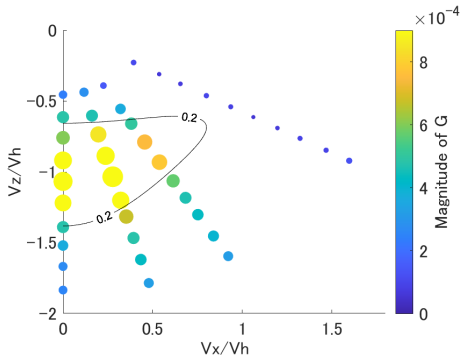

Fig. 9. Comparison of the proposed VRS feature G and the VRS boundary based on ONERA criteria [9]

value is used. In addition, V_z/V_h at the the maximum peak of G is different from the V_z/V_h at the maximum or minimum peak of $\bar{C}_F$ and $\bar{C}_{F\text{std}}$ in the experiment. It may be possible to resolve these problems by using other feature values of the counter torque Q for the detection of the VRS. To make clear the physical mechanism of this difference is one of the future works.

V. Conclusion

The VRS detection method of the UAVs by using counter torque information of the motor is discussed in this paper. The required detection time limit is defined and the VRS detection method which utilizes the low-frequency fluctuation of the estimated propeller motor counter torque as a feature value of the VRS is proposed. The wind tunnel experiments were conducted to measure the thrust and the counter torque at the VRS and to validate the proposed VRS detection method. The thrust reduction and thrust fluctuation increase at the VRS are observed in the experiments. The results also show the possibility of detecting the VRS by using the proposed method. To detect the VRS by using counter torque estimation for real-time control of the UVAs is a novel proposal. Although the accuracy and estimation speed need to be improved, the proposed method is useful to improve the safety of UAVs. The following problems remain to be solved.

- The difference between the VRS detection feature value G and thrust reduction, thrust increase peak.
- The selection of the VRS detection feature value G based on a more accurate physical model.
- Establishment of a method for setting appropriate thresholds G_{th}.
- Reduction of the VRS detection time without deteriorating the accuracy of the VRS detection.

To solve these problems, using other physical analyses including Computational Fluid Dynamics (CFD), or using other VRS models may be efficient. The verification of the VRS detection method with an actual multi-rotor UAV and the proposal of a VRS recovery motion control strategy should be also tackled in future studies.

Acknowledgment

The authors would like to thank Professor Kojiro Suzuki who is with the Department of Advanced Energy, Graduate School of Frontier Sciences, The University of Tokyo for letting us use a wind tunnel for our experiments. This work was partly supported by JSPS KAKENHI Grant Number JP23H00175.

References

[1] Y. Nishii, D. Yashiro, K. Yubai, and S. Komada, "Design of a contact-force controller including state feedback controllers for propeller-driven systems," in *IECON 2020 The 46th Annual Conference of the IEEE Industrial Electronics Society*, pp. 136–141, IEEE, 2020.

[2] P. Li, Z. Mao, S. Pang, W. Shi, S. Quan, and Y. Huangfu, "A fuzzy logic control-based energy management strategy for fuel cell/battery uav hybrid power system," in *IECON 2023-49th Annual Conference of the IEEE Industrial Electronics Society*, pp. 1–6, IEEE, 2023.

[3] M. Suzuki, S. Yokota, A. Matsumoto, H. Hashimoto, and D. Chugo, "Position estimation of the drone based on the tensile force of cooperatively towed tube," in *IECON 2018-44th Annual Conference of the IEEE Industrial Electronics Society*, pp. 4294–4299, IEEE, 2018.

[4] Y. Tsuji, D. Yashiro, Y. Kato, S. Bando, K. Yubai, and S. Komada, "Design of a thrust controller for propeller driven systems operating at multiple wind velocities and propeller angular velocities," *IEEJ Journal of Industry Applications*, vol. 12, no. 6, pp. 1060–1067, 2023.

[5] C. Wanniarachchi, P. Wimalaratne, and K. Karunanayaka, "A behavioral model for single leader: Leader-follower drone swarm in leader's failure," in *2023 IEEE 2nd Industrial Electronics Society Annual On-Line Conference (ONCON)*, pp. 1–6, 2023.

[6] Y. Su, P. Yu, M. J. Gerber, L. Ruan, and T.-C. Tsao, "Fault-tolerant control of an overactuated uav platform built on quadcopters and passive hinges," *IEEE/ASME Transactions on Mechatronics*, vol. 29, no. 1, pp. 602–613, 2024.

[7] W. Johnson, "Model for vortex ring state influence on rotorcraft flight dynamics," tech. rep., Ames Research Center, 2005.

[8] P. Makeev, Y. Ignatkin, and A. Shomov, "Numerical study of the main rotor steep descent modes in the vortex ring state area," in *Journal of Physics: Conference Series*, vol. 1925, p. 012004, IOP Publishing, 2021.

[9] J. Jiménez, A. Desopper, A. Taghizad, and L. Binet, "Induced velocity model in steep descent and vortex-ring state prediction," *European Rotorcraft Forum*, 2001.

[10] J. Park, I. Kim, J. Suk, and S. Kim, "Trajectory optimization for takeoff and landing phase of uam considering energy and safety," *Aerospace Science and Technology*, vol. 140, p. 108489, 2023.

[11] A. Andriën and D. Talaeizadeh, "Time and energy efficient descent trajectories for quadcopters that avoid the vortex ring state," in *2022 IEEE Conference on Control Technology and Applications (CCTA)*, pp. 2–8, IEEE, 2022.

[12] A. Talaeizadeh, H. N. Pishkenari, and A. Alasty, "Quadcopter fast pure descent maneuver avoiding vortex ring state using yaw-rate control scheme," *IEEE Robotics and Automation Letters*, vol. 6, no. 2, pp. 927–934, 2021.

[13] S. Ward and T. Fields, "Development and viability of an inverted descent quadrotor for precision aerial delivery," in *AIAA SCITECH 2022 Forum*, p. 2480, 2022.

[14] Y. Wang, A. Li, H. Tian, and S. Yang, "Vortex ring state avoidance control scheme design for nonlinear autonomous helicopter," *Journal of Guidance, Control, and Dynamics*, vol. 45, no. 8, pp. 1546–1553, 2022.

[15] J. McQuaid, A. Kolaei, G. Bramesfeld, and P. Walsh, "Early onset prediction for rotors in vortex ring state," *Journal of Aerospace Engineering*, vol. 33, no. 6, p. 04020081, 2020.

[16] K. Yokota and H. Fujimoto, "Pitch angle control by regenerative air brake for electric aircraft," *IEEJ Journal of Industry Applications*, vol. 11, no. 2, pp. 308–316, 2022.

[17] O. Shetty and M. Selig, "Small-scale propellers operating in the vortex ring state," in *49th AIAA Aerospace Sciences Meeting including the New Horizons Forum and Aerospace Exposition*, p. 1254, 2011.